

## Article

# MWCNTs Decorated with TiO<sub>2</sub> as Highly Performing Filler in the Preparation of Nanocomposite Membranes for Scalable Photocatalytic Degradation of Bisphenol A in Water

Antonio Tursi <sup>1</sup>, Amerigo Beneduci <sup>1,2</sup>, Isabella Nicotera <sup>1,3</sup> and Cataldo Simari <sup>1,3,\*</sup>

<sup>1</sup> Department of Chemistry and Chemical Technologies, University of Calabria, Via P. Bucci, Cubo 15D, 87036 Arcavacata di Rende, Italy; antonio.tursi@unical.it (A.T.); amerigo.beneduci@unical.it (A.B.); isabella.nicotera@unical.it (I.N.)

<sup>2</sup> SIRiA S.r.l.-Servizi Integrati e Ricerche per l'Ambiente, c/o Department of Chemistry and Chemical Technologies, Spin-Off of the University of Calabria, Via P. Bucci, Cubo 15D, 87036 Arcavacata di Rende, Italy

<sup>3</sup> National Reference Centre for Electrochemical Energy Storage (GISEL)—INSTM, Via G. Giusti 9, 50121 Firenze, Italy

\* Correspondence: cataldo.simari@unical.it; Tel.: +39-0984-493385; Fax: +39-0984-492044

**Abstract:** Bisphenol A (BPA), an endocrine-disrupting compound with estrogenic behavior, is of great concern within the scientific community due to its high production levels and increasing concentration in various surface aquifers. While several materials exhibit excellent capacity for the photocatalytic degradation of BPA, their powdered nature and poor chemical stability render them unsuitable for practical application in large-scale water decontamination. In this study, a new class of nanocomposite membranes based on sulfonated polyethersulfone (sPES) and multiwalled carbon nanotubes decorated with TiO<sub>2</sub> nanoparticles (MWCNTs-TiO<sub>2</sub>) were investigated as efficient and scalable photocatalysts for the photodegradation of BPA in aqueous solutions. The MWCNTs-TiO<sub>2</sub> hybrid material was prepared through a facile and inexpensive hydrothermal method and extensively characterized by XRD, Raman, FTIR, BET, and TGA. Meanwhile, nanocomposite membranes at different filler loadings were prepared by a simple casting procedure. Swelling tests and PFG NMR analyses provided insights into the impact of filler introduction on membrane hydrophilicity and water molecular dynamics, whereas the effectiveness of the various photocatalysts in BPA removal was monitored using HPLC. Among the different MWCNTs-TiO<sub>2</sub> content nanocomposites, the one at 10 wt% loading (sP-MT<sub>10</sub>) showed the best photoactivity. Under UV irradiation at 254 nm and 365 nm for 240 min, photocatalytic oxidation of 5 mg/L bisphenol A by sP-MT<sub>10</sub> resulted in 91% and 82% degradation, respectively. Both the effect of BPA concentration and the membrane regenerability were evaluated, revealing that the sP-MT<sub>10</sub> maintained its maximum BPA removal capability over more than 10 cycles. Our findings indicate that sP-MT nanocomposite membranes are versatile, scalable, efficient, and highly reusable photocatalysts for the degradation of BPA, as well as potentially for other endocrine disruptors.

**Keywords:** wastewater treatment; bisphenol A (BPA) removal; endocrine-disrupting chemicals; MWCNTs-TiO<sub>2</sub> hybrid; nanocomposite membranes; visible-light photodegradation



**Citation:** Tursi, A.; Beneduci, A.; Nicotera, I.; Simari, C. MWCNTs Decorated with TiO<sub>2</sub> as Highly Performing Filler in the Preparation of Nanocomposite Membranes for Scalable Photocatalytic Degradation of Bisphenol A in Water. *Nanomaterials* **2023**, *13*, 2325. <https://doi.org/10.3390/nano13162325>

Academic Editors: Eugenia Fagadar-Cosma, Sherif A. El-Safty, Mihaela Birdeanu, Isabela Costinela Man and Serban Stamatin

Received: 30 July 2023

Revised: 10 August 2023

Accepted: 11 August 2023

Published: 13 August 2023



**Copyright:** © 2023 by the authors. Licensee MDPI, Basel, Switzerland. This article is an open access article distributed under the terms and conditions of the Creative Commons Attribution (CC BY) license (<https://creativecommons.org/licenses/by/4.0/>).

## 1. Introduction

Nowadays, the global water system is highly compromised by poor sanitation, the absence of clean and safe resources, and the huge impact of chemicals, such as dyes, carcinogenic hydrocarbons, heavy metals, organic compounds, and pesticides, which undermine human health and the whole environment [1]. Most of these compounds generate serious repercussions on the systems of living beings; in particular, the endocrine-disrupting compounds (EDCs) alter the endocrine system, thereby creating havoc on biological systems [2]. These compounds have been constantly released into aquatic environments

through different pathways: wastewater discharges, environmental leaching, diffusion through atmospheric phenomena, etc. [3]. To face the issues above, numerous water remediation technologies have been developed. For instance, natural materials and metal organic frameworks (MOFs) are widely acknowledged within the scientific community for their substantial potential across various applications. Notably, the utilization of natural substrates, including biochar [4,5], cellulose [6], activated carbon [7], and hyper-cross-linked polymers (HCP) [8], among others, demonstrates a robust adsorption capacity for diverse pollutant classes, such as fluorides [9,10], organic compounds, persistent organic pollutants (POPs) [11], dyes [12,13], and metals [14–16].

Among the EDCs, bisphenol A (BPA) stands out as a highly representative compound. Notably, BPA exhibits estrogenic characteristics and has garnered significant attention due to its high production, wide applications, and consistently high concentrations in various surface aquifers [17]. Bisphenol A, also known as 2,2-bis(4-hydroxyphenyl)propane, is a synthetic phenolic compound commonly utilized as an additive, flame retardant, or starting monomer for the production of epoxy resins and polycarbonate. Since the 1940s, BPA has found extensive use in the industrial production of plastic containers, DVDs, can linings, and thermal papers. The global production of BPA reaches approximately 8 million tons, solidifying its status as one of the most highly produced chemicals worldwide [18,19]. Additionally, the degradation processes of polyurethane plastics can lead to the release of BPA into the environment [20,21].

A major source of BPA is identified as flows from wastewater treatment plants to groundwater, leading to its spread to secondary sources, such as groundwater, surface water, and soil. Other sources are identified from untreated sewage and sludge use from WWTP in cropland, etc. [22,23]. Moreover, the escalating volumes of industrial and household waste deposited in landfills contribute to a mounting generation of landfill leachates containing elevated BPA concentrations (reaching up to 4500 µg/L), which subsequently infiltrate surface water and groundwater. Overall, BPA concentrations in groundwater range from  $0.09 \times 10^{-3}$  to about 230 µg/L [22]. For example, high concentrations of BPA have also been found in waste paper recycling plants (up to 370 µg/L) [24] and in bottled water in France (0.07–4.21 µg/L) [25]. In many cases, the maximum allowable concentrations of BPA for drinking water, set by government organizations and countries, have even been exceeded. Unfortunately, a critical issue that is difficult to solve immediately is due to the fact that many underdeveloped regions, such as Latin America and Africa, currently do not yet have a regulation for these EDCs in the aquifer sector [22]. All in all, a huge risk of long-term exposure of humans to BPA exists mostly due to the fact that current treatment technologies fail in completely removing this compound from drinking water [26]. Consequently, a relatively vast literature exists about the correlation between BPA exposure and effects on health: metabolic disorders, such as neurotoxicity, obesity, infertility, and precocious puberty, immune system alterations, and interference in cell development are all related to BPA absorption into the body. Furthermore, it has been demonstrated that cardiovascular disease, diabetes in adults, and endometrial hyperplasia are other disorders associated with BPA exposure [27]. In view of such serious problems that the diffusion and adsorption of BPA causes to humans, several technologies have been studied for BPA removal, including coagulation/flocculation/sedimentation/filtration [28–30], carbon nanomaterials (CNMs) (e.g., carbon nanotubes (CNTs)) [31,32] and graphene oxides (GOs) [33,34]), membrane filtration [35,36], ultraviolet (UV) irradiation [37,38], metal-free modification of porphyrin-based porous organic polymers for effective photocatalytic degradation of bisphenol A in water [34], biological processes [39,40], and advanced oxidation techniques [41–43]. However, despite their high sustainability, these materials may experience degradation or a decline in adsorption performance with repeated use cycles. Consequently, the development of an effective and sustainable method to remove BPA from contaminated waters is still a significant challenge for the scientific community.

Against this background, UV degradation is generally considered an effective method for the removal of these classes of contaminants from aqueous media. Moreover, the low

energy consumption, correlated to a high degradation capacity without the use of chemical substances harmful to the environment and human health, hopefully allows for the potential application of this technology on a large scale [44–47]. To date, a large number of emerging photocatalysts have been explored, including Bi<sub>2</sub>WO<sub>6</sub>, Co-doped BiOCl, and Ag<sub>3</sub>PO<sub>4</sub>/rGH, demonstrating excellent photocatalytic activity during the degradation of BPA [48–51]. However, the harsh and costly conditions for their synthesis, combined with the poor chemical stability, limit the usefulness of these catalysts in practical applications. Consequently, titanium dioxide (TiO<sub>2</sub>) is still regarded as the dominant photocatalyst for environmental applications due to its superior photocatalytic oxidation behavior, non-toxicity, low environmental impact, photostability, and inexpensiveness [52]. Unfortunately, the photocatalytic performance of TiO<sub>2</sub> in the bulk form generally suffers from serious catalyst agglomeration, insufficient visible-light absorption, and rapid charge recombination [44,46,53]. For instance, TiO<sub>2</sub> in the anatase form (that is, the phase for TiO<sub>2</sub> exhibiting the highest photocatalytic activity) has a band gap  $E_g$  of about 3.2 eV [54]. This means that  $e^-/h^+$  pairs could be produced only through the absorption of light with a wavelength below 380 nm [55]. In attempting to enhance its light-harvesting efficiency while simultaneously improving the photocatalytic performance, a large number of different strategies have been explored by worldwide researchers, including chemical doping, dye sensitization, and heterojunction construction [44,46,52,53,56]. In the past few years, the design and development of a TiO<sub>2</sub>-hybrid composite photocatalyst have attracted a great amount of research interest. In this regard, due to their prominent structural and electric properties, carbon-based materials, such as graphene, carbon nanotubes, and fullerenes, have demonstrated tremendous potential in extending the photo-response range of TiO<sub>2</sub> to the visible-light region through the modification of the bandgap and/or sensitization [57]. Among them, carbon nanotubes (CNTs) hold great promise due to their capability to conjugate a very large specific surface area with excellent electronic mobility [58]. Indeed, intertwined carbon nanotubes easily generate a highly conductive network with fast interfacial polarization [59], which makes them highly attractive in the enhancement of the visible-light-driven photoactivity of TiO<sub>2</sub>. Ou and co-workers successfully demonstrated that multiwalled carbon nanotubes (MWCNTs) are able to act as photosensitizers in the MWCNTs-TiO<sub>2</sub>:Ni composite catalyst. The latter was then successfully used for photocatalytic H<sub>2</sub> generation under visible light illumination [60]. Dai et al. synthesized a MWCNT-TiO<sub>2</sub> nanohybrid catalyst with visible-light-driven photoactivity through the direct growth of TiO<sub>2</sub> nanoparticles on the surface of the MWCNTs. The hybrid material exhibited high photocatalytic activity under visible light irradiation during the hydrogen generation process [61]. Despite such a huge potential, however, to date and to the best of our knowledge, the use of a MWCNTs-TiO<sub>2</sub> catalyst for the photocatalytic degradation of BPA has been completely inedited. Additionally, during the evaluation of new photocatalytic materials for practical applications, one of the major issues is related to the difficulty in recovering and regenerating the photocatalyst after the photocatalytic process [62–64]. As such, any new materials should be able to provide both good photocatalytic performance and recyclability.

To meet these challenging requirements, we propose the preparation of a composite membrane incorporating a novel MWCNTs-TiO<sub>2</sub> nanohybrid catalyst. This strategy should allow for the combination of the typical advantages of membrane technology, i.e., flexibility, scalability, modular design, and ease in preparation and maintenance, with the photocatalysis, thus providing the most appropriate solution to the industrial requirements for large-scale application. It is noteworthy that the composite membrane can be easily removed from water and regenerated for reuse after the photocatalytic process. To date, only very few studies have reported the use of nanocomposite membranes with photocatalytic activity obtained through the incorporation of TiO<sub>2</sub> [65,66] or TiO<sub>2</sub>-based nanostructures [67], and the approach has been demonstrated to be very promising. Furthermore, it was recently demonstrated that the degradation of water pollutants, specifically dye molecules, can be further enhanced by using sulfonated polymers as the hosting matrix due to a synergistic effect of adsorption and photocatalytic reaction [68,69]. Based on the

above, in this study, the sulfonated derivative of polyethersulfone (sPES) was selected as the hosting matrix on account of its low cost, large commercial availability, low environmental impact, excellent film-forming ability, and superior chemical and thermo-mechanical resistance [70]. Chlorosulfonic acid was used as the sulfonating agent because it allowed for fast and relatively easy reaction control. Also, this synthetic approach is generally free from side reactions and cleavage of the polymer backbone [71]. The reaction was finely controlled in order to reach an ion exchange capacity (IEC) of circa 3 meq/g. At this IEC, the best compromise between good hydrophilicity and mechanical robustness is generally achieved [70]. Therefore, in this work, the MWCNTs-TiO<sub>2</sub> hybrid material was first prepared through the most popular hydrothermal method by using titanium(IV) butoxide as a relatively inexpensive titanium source, and it was tested for its potential in BPA removal from aqueous solutions. To clarify the microstructural and chemical properties of the hybrid material, SEM, XRD, Raman, FTIR, TGA, and porosimetry analyses were carried out, demonstrating that the surface of the MWCNTs was successfully decorated with TiO<sub>2</sub> nanoparticles. Thereafter, sPSU/MWCNTs-TiO<sub>2</sub> nanocomposite membranes at various filler loadings were prepared by simple solution intercalation. The mechanical performance of the nanocomposite membranes was investigated by dynamic mechanical analysis, while their hydrophilic behavior was characterized by swelling tests and the Pulse Field Gradient NMR method. The latter technique allowed for direct measurement of the self-diffusion coefficients, thus providing crucial information on the effect of the filler introduction on the microstructure of the water-filled cluster of the resulting nanocomposites. The photocatalytic degradation of BPA was carried out by batch tests using different experimental conditions (variation of wavelength of UV rays, catalyst dose, initial concentration of BPA, etc.). Additionally, the possibility of reusing the nanocomposite membranes after numerous cycles of degradation was also evaluated. The preliminary results demonstrated that the preparation of sPSU/MWCNTs-TiO<sub>2</sub> nanocomposite membranes could be exploited as a simple, scalable, effective, low-cost, and low-impact method to remove BPA from primary and secondary sources of contamination in various surface water compartments. As such, this study is of great importance for the protection of health in both humans and the environment.

## 2. Materials and Methods

### 2.1. Materials

The following reactants were all supplied by Sigma-Aldrich (Sigma-Aldrich, Milan, Italy) and used without any further purification/modification: Multi-walled carbon nanotubes (MWCNTs, powder with particle size <20 nm), titanium(IV) butoxide (reagent grade, 97%), N,N-dimethylacetamide (anhydrous, 99.8%), sulfuric acid (95–97 wt%), isopropyl alcohol (ACS reagent, ≥99.5%), and nitric acid (65 wt%).

The sPES was synthesized according to the procedure reported elsewhere [70], and the experimental conditions were finely adjusted to achieve an ion exchange capacity of 3.19 meq/g.

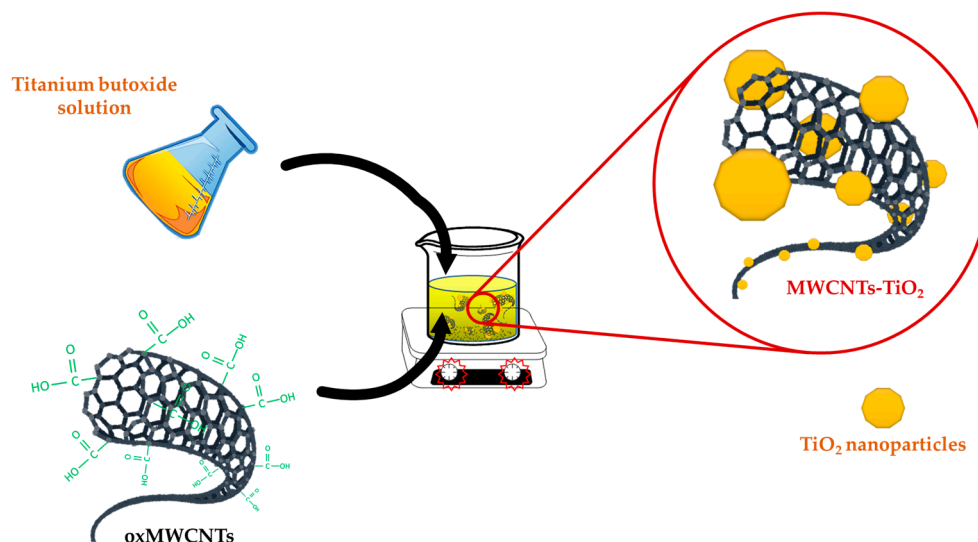
### 2.2. Oxidation of Multi-Walled Carbon Nanotubes (oxMWCNTs)

Pristine MWCNTs were suspended in a H<sub>2</sub>SO<sub>4</sub>/HNO<sub>3</sub> mixture (3:1 v/v) and subjected to sonication for 3 h at RT. Finally, the dispersion was centrifuged, washed several times with deionized water, and dried in an oven at 60 °C overnight to recover the oxidized MWCNTs (oxMWCNTs) in a fine powder.

### 2.3. Surface Decoration of MWCNTs with Titania Nanoparticles (MWCNTs-TiO<sub>2</sub>)

A one-pot hydrothermal method was exploited to synthesize a MWCNTs-TiO<sub>2</sub> hybrid material. Titanium(IV) butoxide was used as a Titania precursor [72], and the synthesis pathway is illustrated in Scheme 1. In a beaker, titanium(IV) butoxide was mixed with nitric acid, isopropyl alcohol, and water, and the reaction was heated at 60 °C using an oil bath. After 1 h of stirring, a titanium(IV) ionic (Ti<sup>4+</sup>) solution was formed. Subsequently,

a homogenous aqueous dispersion of oxidized MWCNTs was gradually added, and the mixture was stirred at 60 °C for an additional 18 h. The molar ratio between the titanium butoxide and GO was 14:1 (*w/w*). The reaction was quenched by pouring it into ice-cold ethanol. Following centrifugation (15,000 r/min), the MWCNTs-TiO<sub>2</sub> hybrid material was recovered as a fine black powder, which underwent several washes with deionized water before being vacuum dried at 60 °C overnight.



**Scheme 1.** Experimental procedure for the synthesis of the MWCNTs-TiO<sub>2</sub> nano hybrid material.

#### 2.4. Preparation of the Nanocomposite Membranes

Nanocomposite membranes were prepared using a straightforward solution-casting procedure [73]. A pristine membrane was prepared by dissolving sPES powder in *N,N*-dimethylacetamide (15 wt% solution). Once a clear solution was achieved, it was cast onto a Petri dish and introduced into an oven set at 60 °C, allowing complete solvent evaporation. Nanocomposite membranes were prepared by directly incorporating the MWCNTs-TiO<sub>2</sub> nano hybrid into the sPES-DMAc polymer solution. To obtain a macroscopically homogeneous dispersion, vigorous mechanical stirring and sonication were alternated for 2 days at room temperature. The loading of the filler ranged from 1 to 10% by weight with respect to the polymer. It should be noted that membranes with higher filler contents exhibited inhomogeneity and brittleness due to particle agglomeration. The final dispersion was then cast on a Petri dish at 60 °C until complete evaporation of the solvents. The resultant membranes were designated as sP-MT<sub>1</sub>, sP-MT<sub>5</sub>, and sP-MT<sub>10</sub> according to the filler amount, i.e., 1, 5, and 10 wt%, respectively. Before the characterizations, all membranes underwent chemical activation in a 1 M H<sub>2</sub>SO<sub>4</sub> solution at 60 °C for 15 h followed by thorough rinsing in deionized water to eliminate any residual traces of acid. All the sPES-based membranes had a dry thickness of 55 ± 5 μm.

#### 2.5. Characterization

X-ray diffraction (XRD) measurements were carried out on a Bruker AXS Diffractometer/Reflectometer (D8) furnished with a Dynamic Scintillation Detector, NaI, and a Gobel mirror. The XRD spectra were acquired using the Cu-K $\alpha$  radiation in transmission mode on powder samples. Prior to analysis, the powders were meticulously inserted into glass capillaries ( $\phi = 1$  mm, Hilgenberg GmbH, Strauchgraben, Malsfeld, Deutschland), which were then positioned in a sample holder [74,75]. Spectra were collected at room temperature within the  $2\theta$  range of 5° to 40°, with increments of 0.03° and a counting time of 1 s/step.

The FTIR spectra were recorded using a Perkin-Elmer Spectrum GX instrument (Perkin-Elmer, Waltham, MA, USA) with KBr pellets. The acquisition encompassed the range of

400–3600  $\text{cm}^{-1}$  at 2  $\text{cm}^{-1}$  resolution, achieved by averaging 64 scans. This allowed for the improvement of the signal-to-noise ratio [76].

Raman spectra were acquired on a Jobin Yvon micro-Raman LABRAM apparatus (Horiba Ltd., Kyoto, Japan) using the 632.8 nm wavelength of a He–Ne laser as the excitation source. Equipped with a 50 $\times$  Olympus lens objective (focal length of 15 mm), the instrument power was about 5 mW and focused on a spot of about 5  $\mu\text{m}$  in diameter. The Raman spectra were gathered within the 200 and 3900  $\text{cm}^{-1}$  range. Changes in the Raman spectra were used to explore molecular-level interactions within the MWCNTs-TiO<sub>2</sub> derivatives [77].

A TG-7 instrument from Perkin-Elmer was employed for thermogravimetric analyses (TGA). Samples were first dried at 60  $^{\circ}\text{C}$  for 24 h and then positioned in an alumina crucible. The heating process took place over a temperature range of 50–900  $^{\circ}\text{C}$  at a rate of 10  $^{\circ}\text{C}/\text{min}$ , utilizing flowing nitrogen [78].

N<sub>2</sub> adsorption/desorption isotherms were acquired at 77 K via a Micromeritics ASAP 2460 apparatus (Micromeritics Instrument Corporation, Norcross, GA, USA). Before each adsorption measurement, the sample underwent outgassing at 473 K for 12 h. Density Functional Theory (DFT) was used to calculate the pore size distributions (PSD) [79].

A Bruker AVANCE 300 wide-bore spectrometer (Bruker Corporation, Billerica, MA, USA) working at 300 MHz on <sup>1</sup>H was used for the NMR measurements. The instrument was equipped with a Diff30 Z-diffusion 30 G/cm/A multinuclear probe with substitutable RF inserts. In particular, a pulsed field gradient stimulated-echo (PFG-STE) sequence [80] was used to obtain a direct measurement of the self-diffusion coefficients (*D*) of water confined within the hydrophilic clusters of the various membranes. For this set of experiments, the Pulse gradient length ( $\delta$ ) was 0.8 ms, while the diffusion delay time ( $\Delta$ ) was 8 ms. The gradient amplitude (*g*) ranged from 80 to 800 G/cm. The uncertainties in *D* values were calculated to be circa 3% on the basis of the very low standard deviation of the fitting curve and the repeatability of the measurements. Diffusivity measurements were collected under increasing temperature in the range of 20–130  $^{\circ}\text{C}$  each 20  $^{\circ}\text{C}$ , with 15 min as the equilibration time for each temperature. Details on the NMR sample preparation can be found elsewhere [81].

The thermomechanical performance of the membranes was investigated using dynamic mechanical analysis (DMA) on a Metravib DMA/25 analyzer (Metravib Limonest, France) equipped with a shear jaw for clamping the films [82–84]. Rectangularly shaped samples were directly cut from the membranes and subjected to a dynamic stress of amplitude 10<sup>−4</sup> at 1 Hz. The temperature ranged from 25 to 180  $^{\circ}\text{C}$ , with a heating rate of 2  $^{\circ}\text{C}/\text{min}$ .

## 2.6. BPA Analytical Determination

The bisphenol A concentration in the filtrate samples was measured by means of a high-performance liquid chromatography (HPLC) system coupled with a diode array detector (SPD-20A Prominence UV Detector, SIL-20AC Prominence autosampler, CTO-20AC Prominence Column oven, DGU-20A5 Prominence degasser, LC-20AT pump, Shimadzu, Tokyo, Japan). The samples were separated by reverse phase (RP) chromatography using a C18 Luna (Phenomenex, Torrance, CA, USA) column (5  $\mu\text{m}$ , 250  $\times$  4.6 mm). The HPLC method was obtained by Tursi et al. [85]. The mobile phase was a mixture of water/acetonitrile (35/65, *v/v*) at a flow rate of 1 mL/min using a UV wavelength at 227 nm. The solvents were eluted isocratically, and the injection volume was kept at 20  $\mu\text{L}$ . A calibration curve was prepared for the quantification of BPA in water by using standards at different concentrations (from 0.5 ppm to 50 ppm). No traces of byproducts amenable to polymer degradation and/or the release of impurities from the MWCNTs-TiO<sub>2</sub> nanomaterial were detected by HPLC analysis.

### 2.7. Preliminary Photocatalytic Degradation Experiments of BPA in Aqueous Batches

The photocatalytic activity of the MWCNTs-TiO<sub>2</sub> membranes was studied by carrying out several batch experimental runs. The experimental temperature was 20 °C. The surface of the MWCNTs-TiO<sub>2</sub> membranes was approximately 2.5 cm<sup>2</sup>. In order to evaluate the photocatalytic performances of MWCNTs-TiO<sub>2</sub> membranes, preliminary tests were conducted under the irradiation of a suitable UV lamp (6 W, 254 nm–365 nm) at a distance of 5 cm from the aqueous batch polluted with different initial concentrations of BPA ranging from 5 to 50 ppm (V = 50 mL, pH = 5.5). During the UV light irradiation experiments, constant stirring at 100 rpm was maintained by an orbital stirring plate (Orbital Platform Shaker, PSU-10i, Grant Instruments, Cambridge, UK) to ensure the tested solution was homogeneous.

A preliminary investigation of BPA degradation was carried out using different experimental conditions in order to evaluate the degradation efficiency of UV rays at 254 and 365 nm. Further tests were conducted in order to evaluate the effect of the dose (%) of TiO<sub>2</sub> catalyst on the membranes and the effect of the initial concentration of BPA on its degradation under UV light. All batch tests were performed under the same conditions of volume (V = 50 mL) and pH (5.5).

During all tests, a fixed amount of sample was withdrawn from polluted batches at different time intervals over 240 min and analyzed according to the method reported in the previous paragraph. All experiments were repeated three times to observe the reproducibility of the measurements, allowing for the attribution of a standard deviation. The removal efficiency (RE%) of the treatments was calculated using the following equation (Equation (1)):

$$\text{RE\%} = \text{Percentage photodegradation of BPA} = \frac{C_0 - C}{C_0} \times 100 \quad (1)$$

where “C<sub>0</sub>” is the initial concentration of BPA and “C” is the concentration of BPA at time ‘t’.

## 3. Results and Discussion

### 3.1. Characterization of the MWCNTs-TiO<sub>2</sub> Nanohybrid

The XRD patterns of oxidized MWCNTs and MWCNTs-TiO<sub>2</sub> materials are depicted in Figure 1. The oxMWCNTs exhibit distinctive diffraction peaks at  $2\theta = 26.2^\circ$  (002) and  $2\theta = 43.5^\circ$  (100), which are attributed to the hexagonal honeycomb structure of carbon nanotubes [86]. In contrast, the X-ray diffraction pattern of the hybrid material displays several additional peaks, indicating the successful growth of TiO<sub>2</sub> onto the CNTs' surface. Notably, a sharp peak at  $2\theta = 25.1^\circ$  (101) indicates the presence of a crystalline anatase phase in the synthesized TiO<sub>2</sub> particles. Peaks at (004), (200), (105), (211), and (204) further confirm that all of the crystal phases are anatase, because no peak of rutile appears [72]. The broadening of the (101) anatase peak was employed to calculate the average crystal size using the Scherrer equation [87], giving an average grain size of ca. 80 nm for TiO<sub>2</sub>. Likely, the presence of MWCNTs hinders direct grain-to-grain contact, resulting in the formation of such a small crystal size of Titania particles in the hybrid MWCNTs-TiO<sub>2</sub> material.

The Raman analysis (Figure 2) further validates the successful formation of the MWCNTs-TiO<sub>2</sub> nanohybrid. Indeed, the Raman pattern of MWCNTs-TiO<sub>2</sub> exhibits characteristic bands of carbon nanotubes (namely, the D-band and G-band at 1345 and 1596 cm<sup>-1</sup> [88], respectively), along with signals corresponding to anatase TiO<sub>2</sub>. These anatase TiO<sub>2</sub> signals encompass E<sub>g(1)</sub>, E<sub>g(2)</sub>, B<sub>1g</sub>, A<sub>1g</sub> + B<sub>1g</sub>, and E<sub>g(2)</sub> modes [89]. It is worth noting that the latter signals display a slight shift compared to the typical bands of pure TiO<sub>2</sub>, confirming the chemical nature of the interaction between the MWCNTs and the TiO<sub>2</sub> heterojunction composite [90].

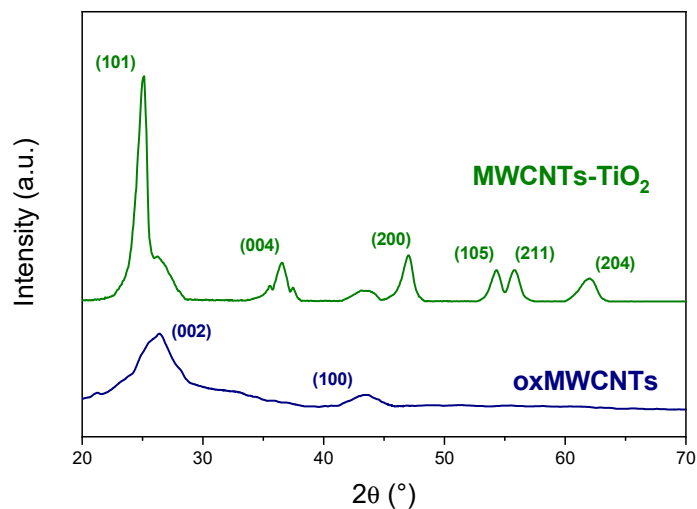


**Figure 1.** XRD patterns of oxMWCNT and MWCNT-TiO<sub>2</sub> materials.

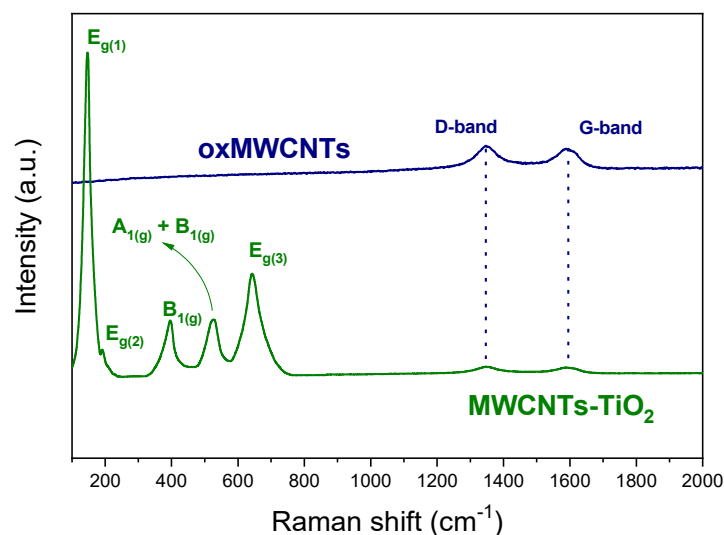


**Figure 2.** Raman spectra of oxMWCNT and its functionalized derivative.

The FTIR analysis was carried out to definitively confirm the nature of the interaction of MWCNTs with TiO<sub>2</sub> nanoparticles. Figure 3 juxtaposes the FTIR spectrum of the hybrid material with that of parental oxMWCNTs in the wavenumber range of 400–3750 cm<sup>-1</sup>. The spectrum of MWCNTs reveals clear evidence of oxygen-containing functional groups resulting from oxidation in sulfuric/nitric acid [91]. Indeed, signals at 1070 and 1240 cm<sup>-1</sup> correspond to epoxy (C-O, C-O-C) groups, while the adsorption bands at 1384, 1745, and 3380 cm<sup>-1</sup> prove the presence of hydroxyl (C-OH) and carboxylic (-C-OOH) groups on the surface of MWCNTs. As can be seen, following the immobilization of TiO<sub>2</sub> nanoparticles on the MWCNT sidewalls, the intensity of the characteristic resonance for carboxylic functionalities decreases, suggesting their consumption during the reaction with the Titania precursor. This undeniably proves the covalent linkage between oxidized MWCNTs and Titania, which likely results from the esterification between the COOH of oxidized MWCNTs and the -OH of TiO<sub>2</sub> [92]. In addition, two absorbance resonances at 460 cm<sup>-1</sup> and 530 cm<sup>-1</sup> appear in the spectrum of MWCNTs-TiO<sub>2</sub>, which are credited to Ti-O-C stretching and the Ti-O-Ti vibration modes, respectively [93].

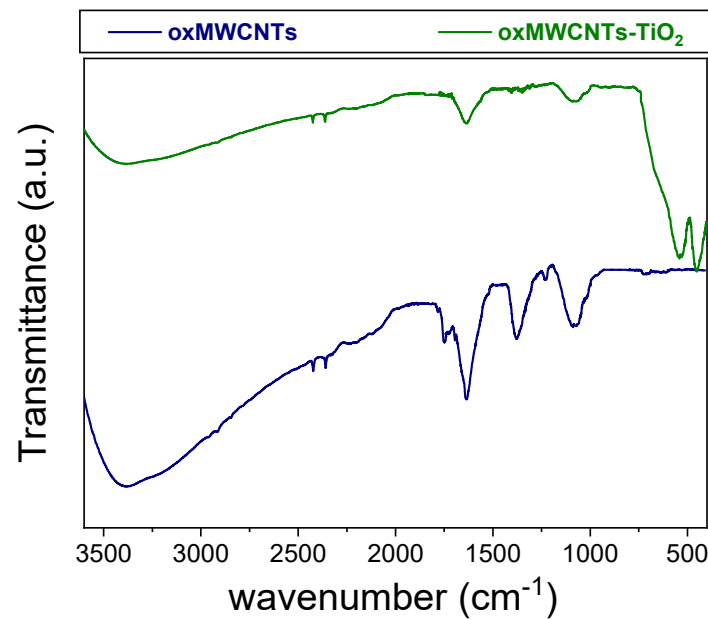
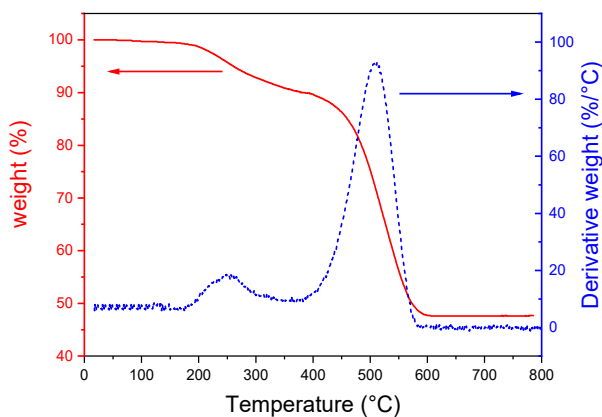
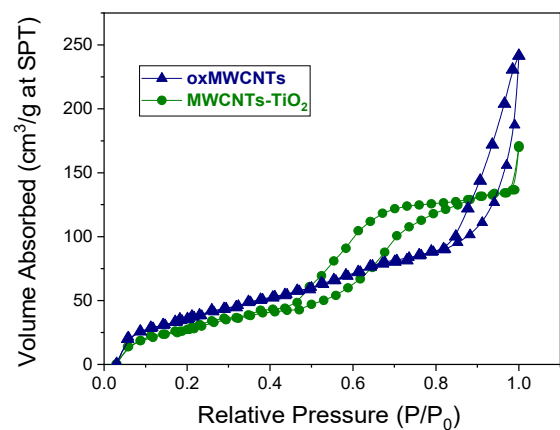


**Figure 3.** FTIR spectra of oxMWCNTs and MWCNTs-TiO<sub>2</sub> samples.

The thermogravimetric analysis of the TiO<sub>2</sub> derivative of the MWCNTs enabled the estimation of the TiO<sub>2</sub> content in the nanohybrid materials. Figure 4a illustrates TGA and DTG curves in a temperature range of 20–800 °C. The first degradation step for MWCNTs-TiO<sub>2</sub> material starts at ca. 200 °C due to the decomposition of oxygen-containing groups, while the critical temperature for the deterioration of the honeycomb structure is around 500–600 °C. Beyond this temperature range, the residual weight, indicative of TiO<sub>2</sub> content, is 47.6%.



**(a)**



**(b)**

**Figure 4.** (a) TGA-DTG curves representing the thermal decomposition of the MWCNTs-TiO<sub>2</sub> hybrid; (b) N<sub>2</sub> adsorption-desorption isotherms of oxMWCNTs and MWCNTs-TiO<sub>2</sub> samples.

Figure 4b presents the N<sub>2</sub> adsorption-desorption isotherm of the MWCNTs-TiO<sub>2</sub> material in comparison with oxidized MWCNTs. Both samples exhibit typical type IV isotherms, with narrow necks and wider bodies. Notably, oxMWCNTs present a hysteresis loop at a relative pressure ( $P/P_0$ ) ranging between 0.8 and 1.0, whereas it is shifted at a lower relative pressure in the case of MWCNTs-TiO<sub>2</sub>, i.e., 0.45–0.85. This suggests a huge difference in the mesoporous structure of the two materials. Oxidized MWCNTs exhibit a BET surface area of 187 m<sup>2</sup> g<sup>-1</sup>, but it increases until 205 m<sup>2</sup> g<sup>-1</sup> in the hybrid MWCNTs-TiO<sub>2</sub> material due to the anchoring of the TiO<sub>2</sub> nanoparticles. This should enable

higher photocatalytic activity. Conversely, the presence of TiO<sub>2</sub> nanoparticles leads to a reduction in pore diameter, which is 43.11 nm for oxMWCNTs and 9.15 for MWCNTs-TiO<sub>2</sub>.

### 3.2. Nanocomposite Membranes

Following the successful synthesis of the MWCNTs-TiO<sub>2</sub> nanohybrid, its potential as an additive for the preparation of sPES-based nanocomposite membranes for water decontamination was explored. Membranes were prepared via simple solution intercalation, and filler content was varied from 1 to 10 wt% with respect to the polymer to elucidate the effect of the filler content. The SEM investigation revealed that the sPES has a compact and uniform cross section devoid of fractures or defects (see Figure S1). Importantly, the introduction of the MWCNTs-TiO<sub>2</sub> hybrid material does not induce any alteration in the microstructure of the resulting membrane. Even at the highest filler content (i.e., 10 wt%), there is no evidence of particle aggregation, proving that the filler maintains sub-nanometric dimensions. This suggests that the coupling of MWCNTs and TiO<sub>2</sub> prevents the aggregation of TiO<sub>2</sub> particles, thereby preserving their capacity to adsorb/degrade organic pollutants.

For membrane applications in water treatment, adequate mechanical and thermal resistance is imperative. Accordingly, the viscoelastic properties of the sPES-based membranes were investigated by dynamic mechanical analysis (DMA). The temperature evolution of the storage modulus ( $E'$ ) is illustrated in Figure 5a for membranes with varying filler loadings. It is well known that sPES possesses notable mechanical robustness [70], showcasing a substantial storage modulus of approximately 643 MPa. Furthermore, the introduction of the MWCNTs-TiO<sub>2</sub> produces a significant enhancement in the mechanical strength of the nanocomposite membranes. The sP-MT<sub>10</sub> membrane exhibits the highest  $E'$  value, reaching 1345 MPa, which represents a two-fold increase compared to the pristine membrane. It is worth noting that the addition of the nanohybrid material also imparts positive effects on the thermal resistance of the resulting films. The storage modulus remains stable until 200 °C for all the membranes, and then it starts to decrease due to softening of the polymer chains. However, this critical temperature is progressively shifted toward a higher value as the filler content increases. The temperature variation of the  $\tan \delta$  (Figure 5b) better elucidates the relationship between the thermal resistance and the filler content. The  $\tan \delta$  profile is characterized by a single peak in the high temperature region, which is typically attributed to the  $\alpha$  transition ( $T_g$ ) of hydrophilic clusters within the polymer membrane. The  $T_g$  for the pristine sPES is 240 °C, but it increases to 273 °C, as in the case of sP-MT<sub>10</sub>. This substantial enhancement in thermo-mechanical resistance is likely amenable to the peculiar architecture of the MWCNTs-TiO<sub>2</sub> material, which combines the reinforcement features of both very long nanotubes and TiO<sub>2</sub> nanoparticles. As a result, the sP-MT membranes demonstrate a commendable capability to withstand severe operating conditions.

The hydrophilic properties of the various sPES-based membranes were monitored by examining their water uptake and volume swelling, with the results illustrated in Figure 6a. Given the inherently hydrophilic nature of the MWCNTs-TiO<sub>2</sub> material, water uptake increases with filler loading, culminating in a value of 32 wt% for the sP-MT<sub>10</sub>. Intriguingly, the volume swelling exhibits an inverse trend: higher filler content corresponds to reduced volume swelling. Likely, the long CNTs decorated with TiO<sub>2</sub> nanoparticles enable the formation of a physically interconnected network at the microscale. This network minimizes dimensional fluctuations of the hydrophilic clusters in the nanocomposite membranes. Moreover, a deeper understanding of the structure–performance relationship for the sPES-based membranes could be gleaned from the investigation of the water dynamics through direct measurements of the self-diffusion coefficient [94,95]. Figure 6b illustrates the Arrhenius plot, which encompasses the temperature range of 20–130 °C and depicts the diffusion of water within the hydrophilic cluster of the various samples. The amount of water adsorbed is the main factor governing the self-diffusion coefficients [96]. As such, the nanocomposites exhibit higher diffusivity compared to the bare polymer. Additionally,  $D$  increases with the filler content until 5 wt%, and the fastest diffusivity of

$6.29 \times 10^{-7} \text{ cm}^2 \text{ s}^{-1}$  is achieved at  $20^\circ \text{C}$  by the sP-MT<sub>5</sub> membrane. Higher loadings have detrimental effects on water mobility, which is likely due to the progressive obstruction of the hydrophilic channels in the nanocomposite membrane. Indeed, the activation energy ( $E_a$ ) associated with water mobility inside the membranes indicates that sP-MT<sub>10</sub> exhibits the highest  $E_a$  value, i.e., 0.203 eV.

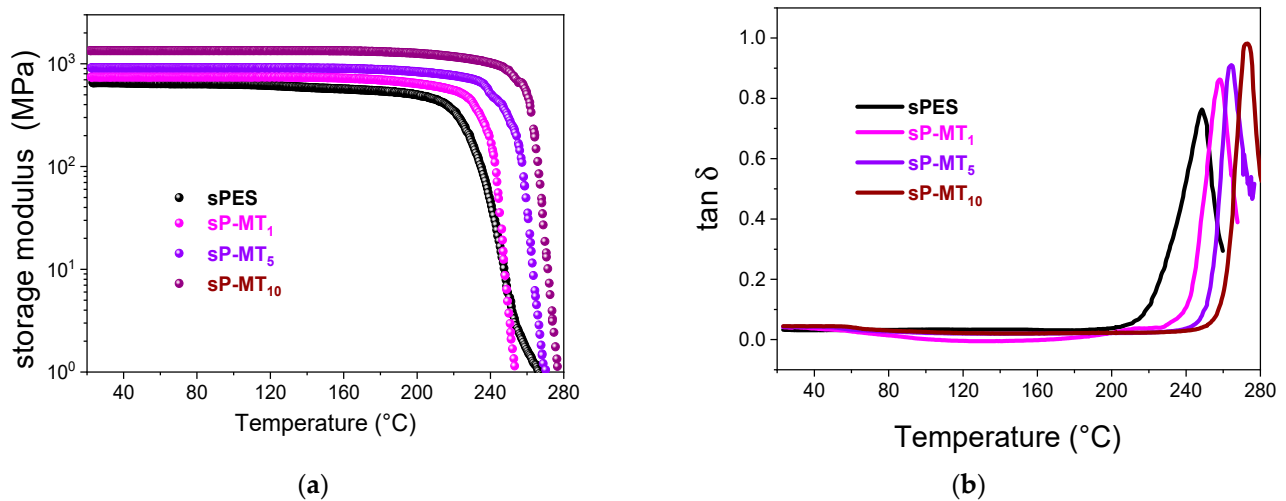


**Figure 5.** Temperature variation of (a) the storage modulus and (b) the tan  $\delta$  for the sPES-based membranes.

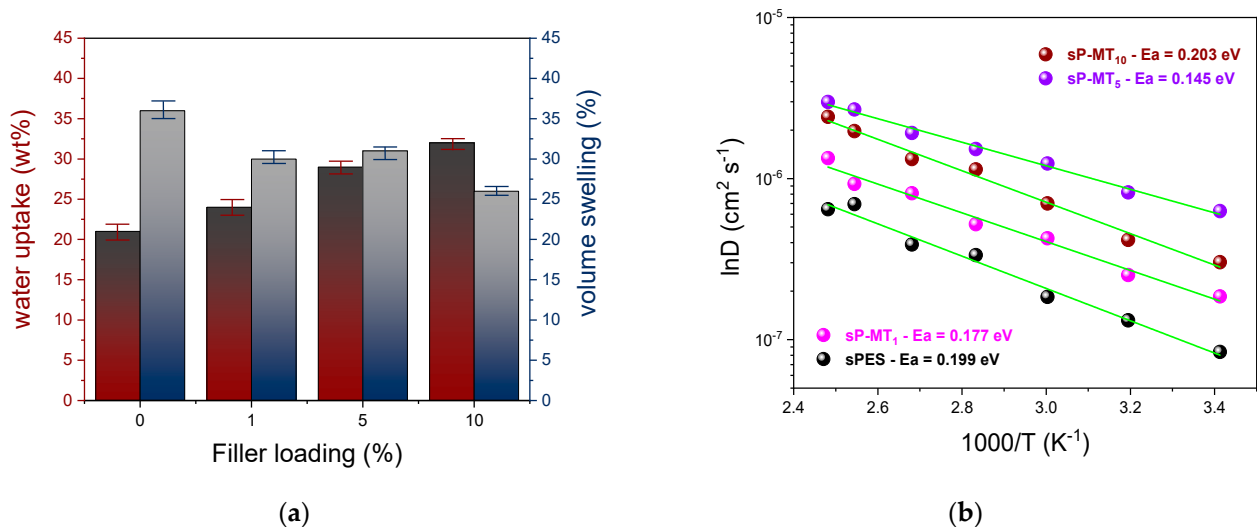


**Figure 6.** (a) Effect of filler content on water uptake and volume swelling of sPES-based nanocomposites; (b) Arrhenius plot of the self-diffusion coefficient values for the sPES and nanocomposite membranes. Green lines in the plot represent linear fitting to the experimental data.

### 3.3. Photocatalytic Degradation of BPA by sP-MT Nanocomposite Membranes

#### 3.3.1. Influence of the Reaction Conditions and MWCNTs-TiO<sub>2</sub> Content on BPA Removal

The preliminary investigation of BPA degradation encompassed a range of experimental conditions to assess the combined impact of the UV light wavelength and the incorporation of the hybrid nano-catalyst on degradation efficiency. In this regard, Figure 7 offers a comparative analysis of the removal efficiency by UV rays only (two different wavelengths were tested, i.e., 254 and 365 nm) with that of sPES and one representative nanocomposite membrane, i.e., sP-MT<sub>1</sub>. In all the batch tests, the experimental parameters were maintained as follows: batch volume = 50 mL, pH = 5.5, and initial concentration of BPA = 5 mg/L. Both the UV light and pristine sPES membrane exhibit inadequate degrada-

tion efficiency, with levels below 15% for BPA degradation after 240 min, regardless of the wavelength used. Nevertheless, the introduction of a minimal amount of MWCNTs-TiO<sub>2</sub> hybrid nanomaterial in the sPES matrix (i.e., 1 wt%) yields a considerable enhancement in removal efficiency. Indeed, BPA degradation escalated from nearly 14% for pristine sPES to an impressive 57% for sP-MT<sub>1</sub> under UV light at 254 nm. This unequivocally underscores the exceptional photocatalytic potential of the MWCNTs-TiO<sub>2</sub> nano hybrid. Xu and coworkers demonstrated that carbonaceous materials decorated with TiO<sub>2</sub> combine three crucial features: (i) an enhanced visible light harvesting, (ii) more efficient charge separation, and (iii) improved adsorption ability for organics [97]. The synergistic effect of these features enables the MWCNTs-TiO<sub>2</sub> material to yield remarkable photocatalytic ability and, thus, high BPA degradation. As expected, degradation efficiency declines using UV light wavelengths at 365 (approximately 41% of BPA degradation). Consequently, to evaluate the effect of the filler content on the BPA removal efficiency, the samples were exposed to UV light at 254 nm.

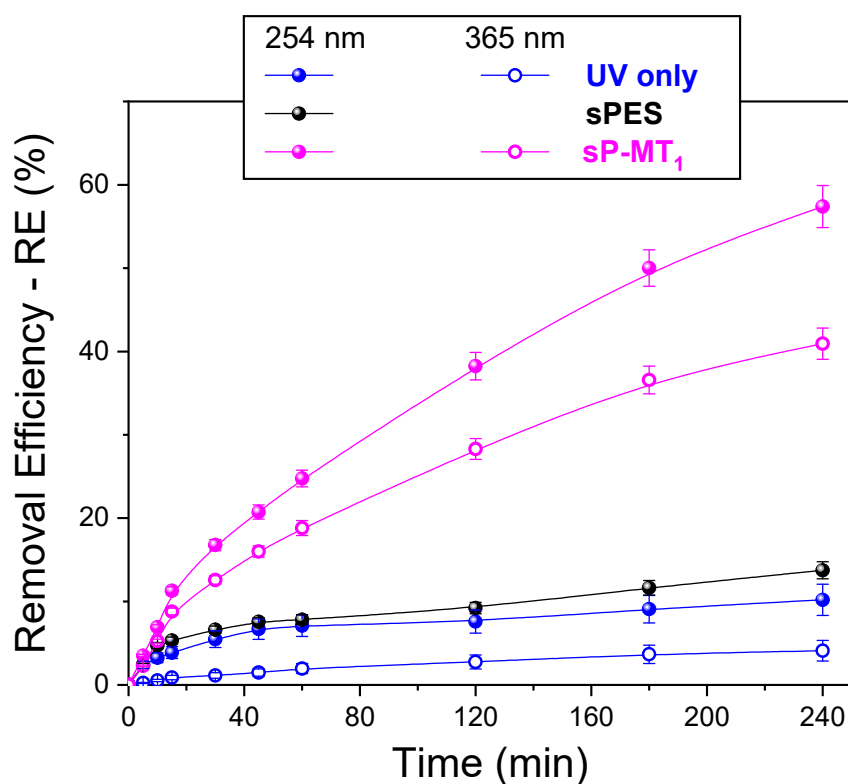


**Figure 7.** Preliminary investigation of BPA degradation for UV light, sPES, and sP-MMT<sub>1</sub>. Experimental conditions: V batch = 50 mL; [BPA] = 5 ppm; pH = 5.5.

As mentioned above, nanocomposite membranes at a higher filler content, i.e., 5 and 10 wt%, were also prepared, and their degradation efficiency was evaluated. Batch tests results with an initial BPA concentration of 5 mg/L (illustrated in Figure 8) show a degradation of BPA in an aqueous solution of 57.4%, 77.6%, and 91.1% after 240 minutes of UV treatment for nanocomposite membranes with 3, 5, and 10 wt% of MWCNT-TiO<sub>2</sub> content, respectively. Moreover, the degradation kinetics also increase considerably with the dose of catalyst into the sPES. Indeed, the photodegradation became more efficient and rapid by increasing the concentration of the photocatalyst dose, going from about 30% for nanocomposite membranes with 1 wt% of nanofiller to 70% for sP-MT<sub>10</sub> after only 120 min of treatment, thus underlining the substantial influence of enhanced active sites. Notably, it is noteworthy that even under UV irradiation at 365 nm, sP-MT<sub>10</sub> achieves substantial BPA degradation of 82% (refer to Figure S2). Last but not least, sP-MT<sub>10</sub> stands in close competition with the current state of the art, where a maximum BPA removal

of 95% was reported after 240 minutes of treatment [98]. However, our nanocomposite membrane has clear competitive advantages, including the low TiO<sub>2</sub> content, ease of recovery, and potential reusability. With the intention of further advancing scientific progress in this field and to offer enhanced solutions, additional investigations into both the effect of BPA concentrations and the reusability of the sP-MT10 nanocomposite membrane were undertaken.

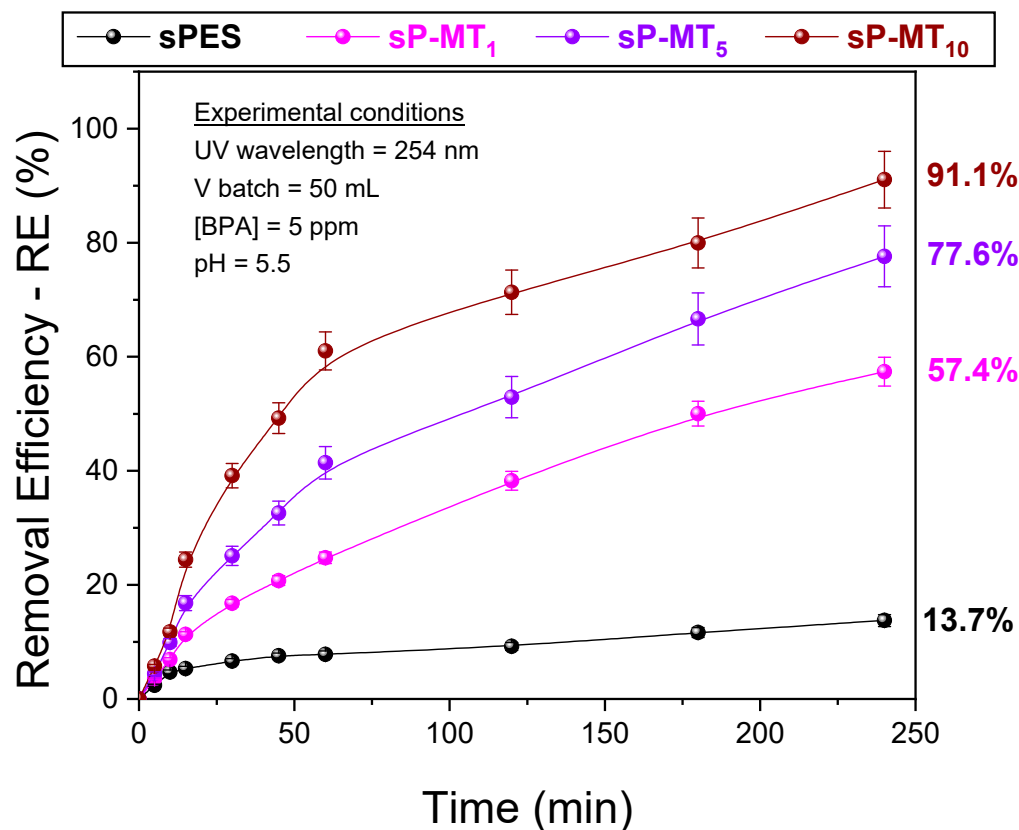
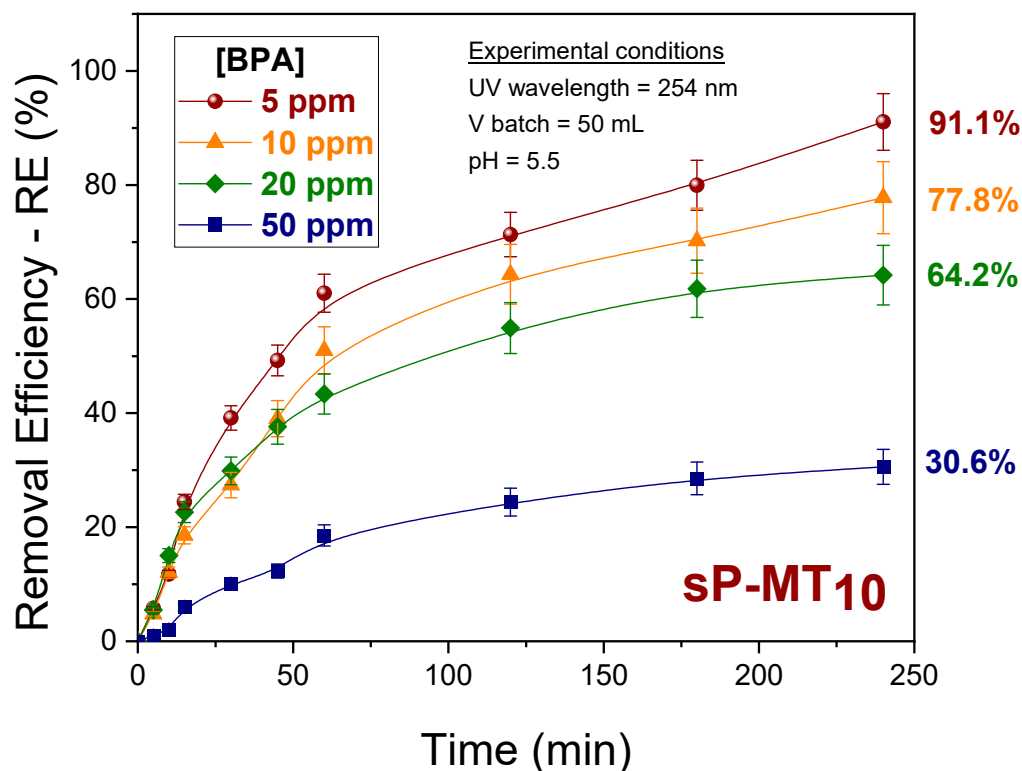


Figure 8. Removal efficiency of BPA as a function of time by sPES-based membranes.

### 3.3.2. Effect of the Initial Concentration of BPA

Exploring the impact of the initial BPA concentration on its degradation under UV light also constituted a focal point of this investigation. A series of experiments were carried out at pH = 5.5 using the sP-MT<sub>10</sub> nanohybrid by subjecting it to 240 min of UV light exposure at a wavelength of 254 nm while varying the initial concentration of BPA from 5 to 50 ppm. The results are illustrated in Figure 9. The outcomes, depicted in Figure 9, underscore a clear dependence of both the extent and rate of BPA decomposition on its initial concentration. Higher BPA concentrations yielded reduced photocatalytic degradation, exemplified by 91.1% degradation for an initial concentration of 5 mg/L, which contrasts with a degradation efficiency of merely 30.6% for a concentration of 50 mg/L. These findings align well with observations made by Garg et al. [99], which indicated significant photolysis of BPA during medium-duration (2–4 h) irradiation. It is plausible that elevated BPA concentrations in the aqueous solution lead to adsorption on the membrane surface, thereby occupying active sites on the TiO<sub>2</sub> catalyst. This phenomenon reduces the generation of hydroxyl radicals and affects the catalytic activity of the photocatalyst. Furthermore, higher BPA concentrations contribute to increased turbidity, consequently reducing the ability to effectively transmit UV light.



**Figure 9.** Removal efficiency of BPA vs. time by sP-MT<sub>10</sub> nanohybrid membrane under different initial concentrations of BPA in water batches, i.e., from 50 to 5 ppm.

### 3.3.3. Regeneration and Reuse of the Nanocomposite Membrane

Considering the significant advantages associated with regeneration and reuse, such as reduced operational costs and minimized environmental impact, regeneration studies play a pivotal role in gauging the feasibility of large-scale application for this treatment methodology. For this purpose, sP-MT<sub>10</sub> was subjected to multiple adsorption/desorption cycles, and its BPA removal efficiency was systematically evaluated. In each cycle, the membrane was removed from the water batch and subjected to a regeneration process involving 20 mL of ethanol (gradient grade for liquid chromatography, LiChrosolv<sup>®</sup>, Sigma-Aldrich) for a period of minutes under orbital stirring at 100 rpm and room temperature. Subsequent washing with distilled water was performed to eliminate any potential ethanol residues on the surface. This treatment allowed for cleaning the active sites of the catalyst, which were possibly covered by impurities generated in the degradation step, and making them available again for the UV degradation processes of BPA. After this simple, fast, and inexpensive treatment, the nanocomposite membrane was once again employed for BPA degradation under identical experimental conditions (initial concentration of BPA of 5 mg/L, pH = 5.5, and UV light at a wavelength of 254 nm). The results shown in Figure 10 unequivocally affirm the exceptional reusability of the nanocomposite membrane, with minimal reduction in its degradation capacity. Upon meticulous analysis, the decrease in degradation performance is negligible—merely 2%—after undergoing 10 consecutive use/regeneration cycles (decreasing from 91.1% to 89.8%). This underscores the remarkable stability and reusability of sP-MT<sub>10</sub>, particularly in contrast to the substantial performance drop of up to 50% reported in most literature materials after only five cycles [98].

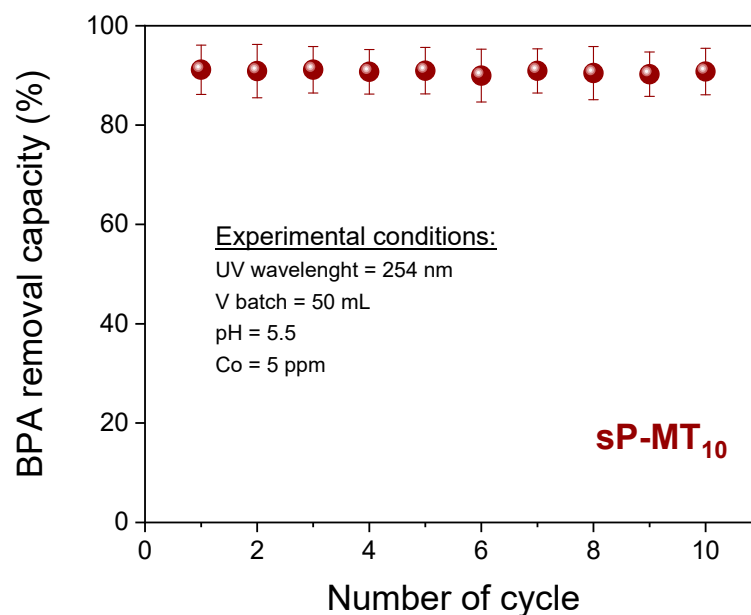


Figure 10. Bisphenol A removal efficiency, RE%, during regeneration and reuse experiments.

#### 4. Conclusions

A MWCNTs-TiO<sub>2</sub> hybrid material was successfully synthesized via a facile hydrothermal method and tested as a nanofiller in a polymeric matrix of sulfonated polyether sulfone (sPES), resulting in the creation of novel nanocomposite membranes. These membranes hold significant promise as an efficient and scalable method for the degradation of bisphenol A (BPA) under visible light. Comprehensive characterization using XRD, Raman, and FTIR techniques has unequivocally established the covalent grafting of TiO<sub>2</sub> nanoparticles onto the MWCNTs surface, thereby confirming the distinctive architecture of the MWCNTs-TiO<sub>2</sub> hybrid material, with a TiO<sub>2</sub> content of 47.6% estimated by TGA analysis. The incorporation of the hybrid material yields substantial enhancements in both the mechanical and hydrophilic properties of the sPES, translating to improved water mobility coupled with exceptional mechanical resistance. Intriguingly, the photocatalytic prowess of the pristine sPES is marginal, but it becomes increasingly substantial with higher filler loading, with sP-MT<sub>10</sub> being able to achieve a BPA degradation of 91% and 82% after 240 min under UV irradiation at 254 nm and 365 nm, respectively. Furthermore, the results of regeneration tests underscore the chemical stability and remarkable reusability of sP-MT<sub>10</sub>. The sorbent can be efficiently regenerated through a swift washing process, showcasing no perceptible decline in BPA removal efficiency even after 10 cycles. Collectively, these findings converge to affirm the tremendous potential of this nanocomposite membrane for practical applications, offering a scalable, efficient, and stable solution for the photodegradation of BPA and/or other endocrine-disrupting chemicals.

**Supplementary Materials:** The following supporting information can be downloaded at: <https://www.mdpi.com/article/10.3390/nano13162325/s1>, Figure S1. Cross-sectional SEM images of the sPES-based membranes at different filler loadings; Figure S2. BPA removal efficiency vs. time for sP-MT<sub>10</sub> at two different UV wavelengths, i.e., 254 and 365 nm.

**Author Contributions:** Conceptualization, C.S.; methodology, C.S. and A.T.; validation, A.B., I.N. and C.S.; formal analysis, C.S. and A.T.; investigation, A.T. and C.S.; resources, A.B. and I.N.; data curation, A.T. and C.S.; writing—original draft preparation, A.T. and C.S.; writing—review and editing, C.S.; visualization, C.S.; supervision, C.S., A.B. and I.N.; project administration, A.B. and I.N.; funding acquisition, A.B. and I.N. All authors have read and agreed to the published version of the manuscript.

**Funding:** This research received no external funding.

**Data Availability Statement:** No new data were created.

**Conflicts of Interest:** The authors declare no conflict of interest.

## References

1. Rath, B.S.; Kumar, P.S.; Vo, D.-V.N. Critical review on hazardous pollutants in water environment: Occurrence, monitoring, fate, removal technologies and risk assessment. *Sci. Total Environ.* **2021**, *797*, 149134. [[CrossRef](#)] [[PubMed](#)]
2. Ohore, O.E.; Songhe, Z. Endocrine disrupting effects of bisphenol A exposure and recent advances on its removal by water treatment systems. A review. *Sci. Afr.* **2019**, *5*, e00135. [[CrossRef](#)]
3. Lim, H.J.; Lee, E.H.; Lee, S.D.; Yoon, Y.; Son, A. Quantitative screening for endocrine-disrupting bisphenol A in consumer and household products using NanoAptamer assay. *Chemosphere* **2018**, *211*, 72–80. [[CrossRef](#)]
4. Obey, G.; Adelaide, M.; Ramaraj, R. Biochar derived from non-customized matamba fruit shell as an adsorbent for wastewater treatment. *J. Bioresour. Bioprod.* **2022**, *7*, 109–115. [[CrossRef](#)]
5. Xin, W.; Wu, Y.; Ma, X.; Wang, A.; Wang, L.; Li, X. Removal of bisphenol A (BPA) by fermented sludge-derived granular biochar from template-like method: From batch experiment to continuous operation. *Process Saf. Environ. Prot.* **2022**, *168*, 239–247. [[CrossRef](#)]
6. Tapia-Orozco, N.; Ibarra-Cabrera, R.; Tecante, A.; Gimeno, M.; Parra, R.; Garcia-Arrazola, R. Removal strategies for endocrine disrupting chemicals using cellulose-based materials as adsorbents: A review. *J. Environ. Chem. Eng.* **2016**, *4*, 3122–3142. [[CrossRef](#)]
7. Sellaoui, L.; Gómez-Avilés, A.; Dhaouadi, F.; Bedia, J.; Bonilla-Petriciolet, A.; Rtimi, S.; Belver, C. Adsorption of emerging pollutants on lignin-based activated carbon: Analysis of adsorption mechanism via characterization, kinetics and equilibrium studies. *Chem. Eng. J.* **2023**, *452*, 139399. [[CrossRef](#)]
8. Zhou, L.; Huang, Q.; Ji, H.; Tang, X.; Zhang, Y.; Chai, K. Efficient adsorption of bisphenol A from water by a hierarchically porous hyper-crosslinked polymer containing  $\beta$ -cyclodextrin polyurethane. *Sep. Purif. Technol.* **2023**, *319*, 124076. [[CrossRef](#)]
9. Jiang, S.; Yang, W. Template-Free Synthesis of Magnetic La-Mn-Fe Tri-Metal Oxide Nanofibers for Efficient Fluoride Remediation: Kinetics, Isotherms, Thermodynamics and Reusability. *Polymers* **2022**, *14*, 5417. [[CrossRef](#)]
10. Jian, S.; Cheng, Y.; Ma, X.; Guo, H.; Hu, J.; Zhang, K.; Jiang, S.; Yang, W.; Duan, G. Excellent fluoride removal performance by electrospun La-Mn bimetal oxide nanofibers. *New J. Chem.* **2022**, *46*, 490–497. [[CrossRef](#)]
11. Naghdi, S.; Shahrestani, M.M.; Zendeabad, M.; Djahaniani, H.; Kazemian, H.; Eder, D. Recent advances in application of metal-organic frameworks (MOFs) as adsorbent and catalyst in removal of persistent organic pollutants (POPs). *J. Hazard. Mater.* **2023**, *442*, 130127. [[CrossRef](#)]
12. Jian, S.; Tian, Z.; Zhang, K.; Duan, G.; Yang, W.; Jiang, S. Hydrothermal Synthesis of Ce-doped ZnO Heterojunction Supported on Carbon Nanofibers with High Visible Light Photocatalytic Activity. *Chem. Res. Chin. Univ.* **2021**, *37*, 565–570. [[CrossRef](#)]
13. Ma, X.; Zhao, S.; Tian, Z.; Duan, G.; Pan, H.; Yue, Y.; Li, S.; Jian, S.; Yang, W.; Liu, K.; et al. MOFs meet wood: Reusable magnetic hydrophilic composites toward efficient water treatment with super-high dye adsorption capacity at high dye concentration. *Chem. Eng. J.* **2022**, *446*, 136851. [[CrossRef](#)]
14. Yang, W.; Wang, Y.; Wang, Q.; Wu, J.; Duan, G.; Xu, W.; Jian, S. Magnetically separable and recyclable Fe<sub>3</sub>O<sub>4</sub>@PDA covalent grafted by L-cysteine core-shell nanoparticles toward efficient removal of Pb<sup>2+</sup>. *Vacuum* **2021**, *189*, 110229. [[CrossRef](#)]
15. Wang, J.; Sun, Y.; Zhao, X.; Chen, L.; Peng, S.; Ma, C.; Duan, G.; Liu, Z.; Wang, H.; Yuan, Y.; et al. A poly(amidoxime)-modified MOF macroporous membrane for high-efficient uranium extraction from seawater. *e-Polymers* **2022**, *22*, 399–410. [[CrossRef](#)]
16. Tursi, A.; Gallizzi, V.; Olivito, F.; Algieri, V.; De Nino, A.; Maiuolo, L.; Beneduci, A. Selective and efficient mercury(II) removal from water by adsorption with a cellulose citrate biopolymer. *J. Hazard. Mater. Lett.* **2022**, *3*, 100060. [[CrossRef](#)]
17. Bhatt, P.; Pathak, V.M.; Bagheri, A.R.; Bilal, M. Microplastic contaminants in the aqueous environment, fate, toxicity consequences, and remediation strategies. *Environ. Res.* **2021**, *200*, 111762. [[CrossRef](#)]
18. Maiuolo, L.; Olivito, F.; Ponte, F.; Algieri, V.; Tallarida, M.A.; Tursi, A.; Chidichimo, G.; Sicilia, E.; De Nino, A. A novel catalytic two-step process for the preparation of rigid polyurethane foams: Synthesis, mechanism and computational studies. *React. Chem. Eng.* **2021**, *6*, 1238–1245. [[CrossRef](#)]
19. Vasiljevic, T.; Harner, T. Bisphenol A and its analogues in outdoor and indoor air: Properties, sources and global levels. *Sci. Total Environ.* **2021**, *789*, 148013. [[CrossRef](#)]
20. Tursi, A.; Baratta, M.; Easton, T.; Chatzisyneon, E.; Chidichimo, F.; De Biase, M.; De Filpo, G. Microplastics in aquatic systems, a comprehensive review: Origination, accumulation, impact, and removal technologies. *RSC Adv.* **2022**, *12*, 28318–28340. [[CrossRef](#)]
21. Maiuolo, L.; Olivito, F.; Algieri, V.; Costanzo, P.; Jiritano, A.; Tallarida, M.A.; Tursi, A.; Sposato, C.; Feo, A.; De Nino, A. Synthesis, characterization and mechanical properties of novel bio-based polyurethane foams using cellulose-derived polyol for chain extension and cellulose citrate as a thickener additive. *Polymers* **2021**, *13*, 2802. [[CrossRef](#)]
22. Dueñas-Moreno, J.; Mora, A.; Cervantes-Avilés, P.; Mahlknecht, J. Groundwater contamination pathways of phthalates and bisphenol A: Origin, characteristics, transport, and fate—A review. *Environ. Int.* **2022**, *170*, 107550. [[CrossRef](#)] [[PubMed](#)]
23. Abraham, A.; Chakraborty, P. A review on sources and health impacts of bisphenol A. *Rev. Environ. Health* **2019**, *35*, 201–210. [[CrossRef](#)]
24. Fukazawa, H.; Watanabe, M.; Shiraishi, F.; Shiraishi, H.; Shiozawa, T.; Matsushita, H.; Terao, Y. Formation of chlorinated derivatives of bisphenol A in waste paper recycling plants and their estrogenic activities. *J. Health Sci.* **2002**, *48*, 242–249. [[CrossRef](#)]

25. Colin, A.; Bach, C.; Rosin, C.; Munoz, J.F.; Dauchy, X. Is drinking water a major route of human exposure to alkylphenol and bisphenol contaminants in France? *Arch. Environ. Contam. Toxicol.* **2014**, *66*, 86–99. [[CrossRef](#)] [[PubMed](#)]
26. Kleywegt, S.; Pileggi, V.; Yang, P.; Hao, C.; Zhao, X.; Rocks, C.; Thach, S.; Cheung, P.; Whitehead, B. Pharmaceuticals, hormones and bisphenol A in untreated source and finished drinking water in Ontario, Canada—Occurrence and treatment efficiency. *Sci. Total Environ.* **2011**, *409*, 1481–1488. [[CrossRef](#)] [[PubMed](#)]
27. Rees Clayton, E.M.; Todd, M.; Dowd, J.B.; Aiello, A.E. The impact of bisphenol A and triclosan on immune parameters in the U.S. population, NHANES 2003–2006. *Environ. Health Perspect.* **2011**, *119*, 390–396. [[CrossRef](#)]
28. Joseph, L.; Flora, J.R.V.; Park, Y.G.; Badawy, M.; Saleh, H.; Yoon, Y. Removal of natural organic matter from potential drinking water sources by combined coagulation and adsorption using carbon nanomaterials. *Sep. Purif. Technol.* **2012**, *95*, 64–72. [[CrossRef](#)]
29. Olivito, F.; Algeri, V.; Jiritano, A.; Tallarida, M.A.; Tursi, A.; Costanzo, P.; Maiuolo, L.; De Nino, A. Cellulose citrate: A convenient and reusable bio-adsorbent for effective removal of methylene blue dye from artificially contaminated water. *RSC Adv.* **2021**, *11*, 34309–34318. [[CrossRef](#)]
30. Barzegari, Z.; Bina, B.; Pourzamani, H.R.; Ebrahimi, A. The combined treatment of bisphenol A (BPA) by coagulation/flocculation (C/F) process and UV irradiation in aqueous solutions. *Desalin. Water Treat.* **2016**, *57*, 8802–8808. [[CrossRef](#)]
31. Joseph, L.; Zaib, Q.; Khan, I.A.; Berge, N.D.; Park, Y.G.; Saleh, N.B.; Yoon, Y. Removal of bisphenol A and 17 $\alpha$ -ethinyl estradiol from landfill leachate using single-walled carbon nanotubes. *Water Res.* **2011**, *45*, 4056–4068. [[CrossRef](#)]
32. Baratta, M.; Mastropietro, T.F.; Bruno, R.; Tursi, A.; Negro, C.; Ferrando-Soria, J.; Mashin, A.I.; Nezhdanov, A.; Nicoletta, F.P.; De Filipo, G.; et al. Multivariate Metal-Organic Framework/Single-Walled Carbon Nanotube Buckypaper for Selective Lead Decontamination. *ACS Appl. Nano Mater.* **2022**, *5*, 5223–5233. [[CrossRef](#)] [[PubMed](#)]
33. Nam, S.W.; Jung, C.; Li, H.; Yu, M.; Flora, J.R.V.; Boateng, L.K.; Her, N.; Zoh, K.D.; Yoon, Y. Adsorption characteristics of diclofenac and sulfamethoxazole to graphene oxide in aqueous solution. *Chemosphere* **2015**, *136*, 20–26. [[CrossRef](#)] [[PubMed](#)]
34. Wang, Y.; Wei, X.; Qi, Y.; Huang, H. Efficient removal of bisphenol-A from water and wastewater by Fe<sub>2</sub>O<sub>3</sub>-modified graphene oxide. *Chemosphere* **2021**, *263*, 127563. [[CrossRef](#)]
35. Muhamad, M.S.; Salim, M.R.; Lau, W.J.; Yusop, Z. A review on bisphenol A occurrences, health effects and treatment process via membrane technology for drinking water. *Environ. Sci. Pollut. Res.* **2016**, *23*, 11549–11567. [[CrossRef](#)] [[PubMed](#)]
36. de Oliveira, L.K.; Moura, A.L.A.; Barbosa, V.; Parreira, R.L.T.; Banegas, R.S.; Caramori, G.F.; Ciuffi, K.J.; Molina, E.F. Removal of the emerging contaminant bisphenol A by an ureasil–PEO hybrid membrane: Experimental study and molecular dynamic simulation. *Environ. Sci. Pollut. Res.* **2017**, *24*, 18421–18433. [[CrossRef](#)]
37. Wang, L.; Zhao, J.; Li, Y. Removal of bisphenol A and 4-n-nonylphenol coupled to nitrate reduction using acclimated activated sludge under anaerobic conditions. *J. Chem. Technol. Biotechnol.* **2014**, *89*, 391–400. [[CrossRef](#)]
38. Duan, X.D.; He, X.X.; Wang, D.; Mezyk, S.P.; Otto, S.C.; Marfil Vega, R.; Mills, M.A.; Dionysiou, D.D. Decomposition of iodinated pharmaceuticals by UV254 nm-assisted advanced oxidation processes. *J. Hazard. Mater.* **2017**, *323*, 489–499. [[CrossRef](#)]
39. Eio, E.J.; Kawai, M.; Niwa, C.; Ito, M.; Yamamoto, S.; Toda, T. Biodegradation of bisphenol A by an algal-bacterial system. *Environ. Sci. Pollut. Res.* **2015**, *22*, 15145–15153. [[CrossRef](#)]
40. Wang, G.; Wu, F.; Zhang, X.; Luo, M.; Deng, N. Enhanced photodegradation of bisphenol A in the presence of  $\beta$ -cyclodextrin under UV light. *J. Chem. Technol. Biotechnol.* **2006**, *81*, 805–811. [[CrossRef](#)]
41. Davididou, K.; Hale, E.; Lane, N.; Chatzisympson, E.; Pichavant, A.; Hochepped, J.F. Photocatalytic treatment of saccharin and bisphenol-A in the presence of TiO<sub>2</sub> nanocomposites tuned by Sn(IV). *Catal. Today* **2017**, *287*, 3–9. [[CrossRef](#)]
42. Rivero, M.J.; Alonso, E.; Dominguez, S.; Ribao, P.; Ibañez, R.; Ortiz, I.; Irabien, A. Kinetic analysis and biodegradability of the Fenton mineralization of bisphenol A. *J. Chem. Technol. Biotechnol.* **2014**, *89*, 1228–1234. [[CrossRef](#)]
43. Zacharakis, A.; Chatzisympson, E.; Binas, V.; Frontistis, Z.; Venieri, D.; Mantzavinos, D. Solar photocatalytic degradation of bisphenol a on immobilized ZnO or TiO<sub>2</sub>. *Int. J. Photoenergy* **2013**, *2013*, 570587. [[CrossRef](#)]
44. Chen, C.; Ma, W.; Zhao, J. Semiconductor-mediated photodegradation of pollutants under visible-light irradiation. *Chem. Soc. Rev.* **2010**, *39*, 4206–4219. [[CrossRef](#)]
45. Wu, Y.; Xing, M.; Zhang, J.; Chen, F. Effective visible light-active boron and carbon modified TiO<sub>2</sub> photocatalyst for degradation of organic pollutant. *Appl. Catal. B Environ.* **2010**, *97*, 182–189. [[CrossRef](#)]
46. Banerjee, S.; Pillai, S.C.; Falaras, P.; O’shea, K.E.; Byrne, J.A.; Dionysiou, D.D. New insights into the mechanism of visible light photocatalysis. *J. Phys. Chem. Lett.* **2014**, *5*, 2543–2554. [[CrossRef](#)]
47. Bora, L.V.; Mewada, R.K. Visible/solar light active photocatalysts for organic effluent treatment: Fundamentals, mechanisms and parametric review. *Renew. Sustain. Energy Rev.* **2017**, *76*, 1393–1421. [[CrossRef](#)]
48. Wang, C.; Zhu, L.; Wei, M.; Chen, P.; Shan, G. Photolytic reaction mechanism and impacts of coexisting substances on photodegradation of bisphenol A by Bi<sub>2</sub>WO<sub>6</sub> in water. *Water Res.* **2012**, *46*, 845–853. [[CrossRef](#)] [[PubMed](#)]
49. Wang, C.Y.; Zhang, Y.J.; Wang, W.K.; Pei, D.N.; Huang, G.X.; Chen, J.J.; Zhang, X.; Yu, H.Q. Enhanced photocatalytic degradation of bisphenol A by Co-doped BiOCl nanosheets under visible light irradiation. *Appl. Catal. B Environ.* **2018**, *221*, 320–328. [[CrossRef](#)]
50. Mu, C.; Zhang, Y.; Cui, W.; Liang, Y.; Zhu, Y. Removal of bisphenol A over a separation free 3D Ag<sub>3</sub>PO<sub>4</sub>-graphene hydrogel via an adsorption-photocatalysis synergy. *Appl. Catal. B Environ.* **2017**, *212*, 41–49. [[CrossRef](#)]
51. Bechambi, O.; Sayadi, S.; Najjar, W. Photocatalytic degradation of bisphenol A in the presence of C-doped ZnO: Effect of operational parameters and photodegradation mechanism. *J. Ind. Eng. Chem.* **2015**, *32*, 201–210. [[CrossRef](#)]

52. Xu, H.; Ouyang, S.; Liu, L.; Reunchan, P.; Umezawa, N.; Ye, J. Recent advances in TiO<sub>2</sub>-based photocatalysis. *J. Mater. Chem. A* **2014**, *2*, 12642–12661. [[CrossRef](#)]
53. Dong, H.; Zeng, G.; Tang, L.; Fan, C.; Zhang, C.; He, X.; He, Y. An overview on limitations of TiO<sub>2</sub>-based particles for photocatalytic degradation of organic pollutants and the corresponding countermeasures. *Water Res.* **2015**, *79*, 128–146. [[CrossRef](#)] [[PubMed](#)]
54. Eddy, D.R.; Permana, M.D.; Sakti, L.K.; Sheha, G.A.N.; Solihudin, G.A.N.; Hidayat, S.; Takei, T.; Kumada, N.; Rahayu, I. Heterophase Polymorph of TiO<sub>2</sub> (Anatase, Rutile, Brookite, TiO<sub>2</sub> (B)) for Efficient Photocatalyst: Fabrication and Activity. *Nanomaterials* **2023**, *13*, 704. [[CrossRef](#)]
55. Carp, O.; Huisman, C.L.; Reller, A. Photoinduced reactivity of titanium dioxide. *Prog. Solid State Chem.* **2004**, *32*, 33–177. [[CrossRef](#)]
56. Spasiano, D.; Marotta, R.; Malato, S.; Fernandez-Ibañez, P.; Di Somma, I. Solar photocatalysis: Materials, reactors, some commercial, and pre-industrialized applications. A comprehensive approach. *Appl. Catal. B Environ.* **2015**, *170–171*, 90–123. [[CrossRef](#)]
57. Leary, R.; Westwood, A. Carbonaceous nanomaterials for the enhancement of TiO<sub>2</sub> photocatalysis. *Carbon* **2011**, *49*, 741–772. [[CrossRef](#)]
58. Wu, B.; Zhu, H.; Yang, Y.; Huang, J.; Liu, T.; Kuang, T.; Jiang, S.; Hejna, A.; Liu, K. Effect of different proportions of CNTs/Fe<sub>3</sub>O<sub>4</sub> hybrid filler on the morphological, electrical and electromagnetic interference shielding properties of poly(lactic acid) nanocomposites. *e-Polymers* **2023**, *23*, 20230006. [[CrossRef](#)]
59. Zhang, Y.; Zhou, W.; Chen, H.; Duan, G.; Luo, H.; Li, Y. Facile preparation of CNTs microspheres as improved carbon absorbers for high-efficiency electromagnetic wave absorption. *Ceram. Int.* **2021**, *47*, 10013–10018. [[CrossRef](#)]
60. Ou, Y.; Lin, J.; Fang, S.; Liao, D. MWNT-TiO<sub>2</sub>:Ni composite catalyst: A new class of catalyst for photocatalytic H<sub>2</sub> evolution from water under visible light illumination. *Chem. Phys. Lett.* **2006**, *429*, 199–203. [[CrossRef](#)]
61. Dai, K.; Peng, T.; Ke, D.; Wei, B. Photocatalytic hydrogen generation using a nanocomposite of multi-walled carbon nanotubes and TiO<sub>2</sub> nanoparticles under visible light irradiation. *Nanotechnology* **2009**, *20*, 125603. [[CrossRef](#)] [[PubMed](#)]
62. Wang, H.; Dong, S.; Chang, Y.; Faria, J.L. Enhancing the photocatalytic properties of TiO<sub>2</sub> by coupling with carbon nanotubes and supporting gold. *J. Hazard. Mater.* **2012**, *235–236*, 230–236. [[CrossRef](#)] [[PubMed](#)]
63. Yao, Y.; Li, G.; Ciston, S.; Lueptow, R.M.; Gray, K.A. Photoreactive TiO<sub>2</sub>/carbon nanotube composites: Synthesis and reactivity. *Environ. Sci. Technol.* **2008**, *42*, 4952–4957. [[CrossRef](#)]
64. Chen, M.L.; Zhang, F.J.; Oh, W.C. Synthesis, characterization, and photocatalytic analysis of CNT/TiO<sub>2</sub> composites derived from MWCNTs and titanium sources. *New Carbon Mater.* **2009**, *24*, 159–166. [[CrossRef](#)]
65. Mau, A.W.H.; Huang, C.B.; Kakuta, N.; Bard, A.J.; Campion, A.; Fox, M.A.; White, J.M.; Webber, S.E.; Mau, A.W.H. H<sub>2</sub> Photoproduction by Nafion/CdS/Pt Films in H<sub>2</sub>O/S<sup>2-</sup> Solutions. *J. Am. Chem. Soc.* **1984**, *106*, 6537–6542. [[CrossRef](#)]
66. Liu, P.; Bandara, J.; Lin, Y.; Elgin, D.; Allard, L.F.; Sun, Y.P. Formation of nanocrystalline titanium dioxide in perfluorinated ionomer membrane. *Langmuir* **2002**, *18*, 10398–10401. [[CrossRef](#)]
67. Lee, J.; Chae, H.R.; Won, Y.J.; Lee, K.; Lee, C.H.; Lee, H.H.; Kim, I.C.; Lee, J. min Graphene oxide nanoplatelets composite membrane with hydrophilic and antifouling properties for wastewater treatment. *J. Memb. Sci.* **2013**, *448*, 223–230. [[CrossRef](#)]
68. Scalese, S.; Nicotera, I.; D'Angelo, D.; Filice, S.; Libertino, S.; Simari, C.; Dimos, K.; Privitera, V. Cationic and anionic azo-dye removal from water by sulfonated graphene oxide nanosheets in Nafion membranes. *New J. Chem.* **2016**, *40*, 3654–3663. [[CrossRef](#)]
69. Filice, S.; D'Angelo, D.; Libertino, S.; Nicotera, I.; Kosma, V.; Privitera, V.; Scalese, S. Graphene oxide and titania hybrid Nafion membranes for efficient removal of methyl orange dye from water. *Carbon* **2015**, *82*, 489–499. [[CrossRef](#)]
70. Simari, C.; Vecchio, C.L.; Enotiadis, A.; Davoli, M.; Baglio, V.; Nicotera, I. Toward optimization of a robust low-cost sulfonated-polyethersulfone containing layered double hydroxide for PEM fuel cells. *J. Appl. Polym. Sci.* **2019**, *136*, 47884. [[CrossRef](#)]
71. Martos, A.M.; Sanchez, J.Y.; Várez, A.; Levenfeld, B. Electrochemical and structural characterization of sulfonated polysulfone. *Polym. Test.* **2015**, *45*, 185–193. [[CrossRef](#)]
72. Simari, C.; Lufrano, E.; Godbert, N.; Gournis, D.; Coppola, L.; Nicotera, I. Titanium dioxide grafted on graphene oxide: Hybrid nanofiller for effective and low-cost proton exchange membranes. *Nanomaterials* **2020**, *10*, 1572. [[CrossRef](#)] [[PubMed](#)]
73. Simari, C.; Lufrano, E.; Rehman, M.H.U.; Zhegur-Khais, A.; Haj-Bsoul, S.; Dekel, D.R.; Nicotera, I. Effect of LDH Platelets on the Transport Properties and Carbonation of Anion Exchange Membranes. *Electrochim. Acta* **2021**, *403*, 139713. [[CrossRef](#)]
74. Nicotera, I.; Kosma, V.; Simari, C.; D'Urso, C.; Aricò, A.S.; Baglio, V. Methanol and proton transport in layered double hydroxide and smectite clay-based composites: Influence on the electrochemical behavior of direct methanol fuel cells at intermediate temperatures. *J. Solid State Electrochem.* **2015**, *19*, 2053–2061. [[CrossRef](#)]
75. de Bonis, C.; Simari, C.; Kosma, V.; Mecheri, B.; D'Epifanio, A.; Allodi, V.; Mariotto, G.; Brutti, S.; Suarez, S.; Pilar, K.; et al. Enhancement of proton mobility and mitigation of methanol crossover in sPEEK fuel cells by an organically modified titania nanofiller. *J. Solid State Electrochem.* **2016**, *20*, 1585–1598. [[CrossRef](#)]
76. Simari, C.; Baglio, V.; Lo Vecchio, C.; Aricò, A.S.; Agostino, R.G.; Coppola, L.; Oliviero Rossi, C.; Nicotera, I. Reduced methanol crossover and enhanced proton transport in nanocomposite membranes based on clay–CNTs hybrid materials for direct methanol fuel cells. *Ionics* **2017**, *23*, 2113–2123. [[CrossRef](#)]
77. Simari, C.; Lufrano, E.; Coppola, L.; Nicotera, I. Composite gel polymer electrolytes based on organo-modified nanoclays: Investigation on lithium-ion transport and mechanical properties. *Membranes* **2018**, *8*, 69. [[CrossRef](#)]

78. Simari, C.; Lufrano, E.; Brunetti, A.; Barbieri, G.; Nicotera, I. Highly-performing and low-cost nanostructured membranes based on Polysulfone and layered doubled hydroxide for high-temperature proton exchange membrane fuel cells. *J. Power Sources* **2020**, *471*, 228440. [[CrossRef](#)]
79. Kupgan, G.; Liyana-Arachchi, T.P.; Colina, C.M. NLDFT Pore Size Distribution in Amorphous Microporous Materials. *Langmuir* **2017**, *33*, 11138–11145. [[CrossRef](#)]
80. Tanner, J.E. Use of the stimulated echo in NMR diffusion studies. *J. Chem Phys.* **1970**, *52*, 2523–2526. [[CrossRef](#)]
81. Simari, C.; Potsi, G.; Policicchio, A.; Perrotta, I.; Nicotera, I. Clay-Carbon Nanotubes Hybrid Materials for Nanocomposite Membranes: Advantages of Branched Structure for Proton Transport under Low Humidity Conditions in PEMFCs. *J. Phys. Chem. C* **2016**, *120*, 2574–2584. [[CrossRef](#)]
82. Simari, C.; Lo Vecchio, C.; Baglio, V.; Nicotera, I. Sulfonated polyethersulfone/polyetheretherketone blend as high performing and cost-effective electrolyte membrane for direct methanol fuel cells. *Renew. Energy* **2020**, *159*, 336–345. [[CrossRef](#)]
83. Simari, C.; Lufrano, E.; Corrente, G.A.; Nicotera, I. Anisotropic behavior of mechanically extruded sulfonated polysulfone: Implications for proton exchange membrane fuel cell applications. *Solid State Ionics* **2021**, *362*, 115581. [[CrossRef](#)]
84. Rehman, M.H.U.; Lufrano, E.; Simari, C. Nanocomposite Membranes for PEM-FCs: Effect of LDH Introduction on the Physico-Chemical Performance of Various Polymer Matrices. *Polymers* **2023**, *15*, 502. [[CrossRef](#)]
85. Tursi, A.; Chatzisyseon, E.; Chidichimo, F.; Beneduci, A.; Chidichimo, G. Removal of endocrine disrupting chemicals from water: Adsorption of bisphenol-a by biobased hydrophobic functionalized cellulose. *Int. J. Environ. Res. Public Health* **2018**, *15*, 2419. [[CrossRef](#)]
86. Wang, W.; Serp, P.; Kalck, P.; Faria, J.L. Visible light photodegradation of phenol on MWNT-TiO<sub>2</sub> composite catalysts prepared by a modified sol-gel method. *J. Mol. Catal. A Chem.* **2005**, *235*, 194–199. [[CrossRef](#)]
87. Huang, X.H.; Zhan, Z.Y.; Wang, X.; Zhang, Z.; Xing, G.Z.; Guo, D.L.; Leusink, D.P.; Zheng, L.X.; Wu, T. Rayleigh-instability-driven simultaneous morphological and compositional transformation from Co nanowires to CoO octahedra. *Appl. Phys. Lett.* **2010**, *97*, 4–6. [[CrossRef](#)]
88. Ramesh Reddy, N.; Mamatha Kumari, M.; Cheralathan, K.K.; Shankar, M.V. Enhanced photocatalytic hydrogen production activity of noble metal free MWCNT-TiO<sub>2</sub> nanocomposites. *Int. J. Hydrogen Energy* **2018**, *43*, 4036–4043. [[CrossRef](#)]
89. Hamid, S.B.A.; Tan, T.L.; Lai, C.W.; Samsudin, E.M. Multiwalled carbon nanotube/TiO<sub>2</sub> nanocomposite as a highly active photocatalyst for photodegradation of Reactive Black 5 dye. *Chin. J. Catal.* **2014**, *35*, 2014–2019. [[CrossRef](#)]
90. Zhou, J.; Zhang, M.; Zhu, Y. Photocatalytic enhancement of hybrid C<sub>3</sub>N<sub>4</sub>/TiO<sub>2</sub> prepared via ball milling method. *Phys. Chem. Chem. Phys.* **2015**, *17*, 3647–3652. [[CrossRef](#)]
91. Simari, C.; Stallworth, P.; Peng, J.; Coppola, L.; Greenbaum, S.; Nicotera, I. Graphene oxide and sulfonated-derivative: Proton transport properties and electrochemical behavior of Nafion-based nanocomposites. *Electrochim. Acta* **2019**, *297*, 240–249. [[CrossRef](#)]
92. Wang, Q.; Yang, D.; Chen, D.; Wang, Y.; Jiang, Z. Synthesis of anatase titania-carbon nanotubes nanocomposites with enhanced photocatalytic activity through a nanocoating-hydrothermal process. *J. Nanoparticle Res.* **2007**, *9*, 1087–1096. [[CrossRef](#)]
93. Fu, J.; Kyzas, G.Z.; Cai, Z.; Deliyanni, E.A.; Liu, W.; Zhao, D. Photocatalytic degradation of phenanthrene by graphite oxide-TiO<sub>2</sub>-Sr(OH)<sub>2</sub>/SrCO<sub>3</sub> nanocomposite under solar irradiation: Effects of water quality parameters and predictive modeling. *Chem. Eng. J.* **2018**, *335*, 290–300. [[CrossRef](#)]
94. Nicotera, I.; Kosma, V.; Simari, C.; Ranieri, G.A.; Sgambetterra, M.; Panero, S.; Navarra, M.A. An NMR study on the molecular dynamic and exchange effects in composite Nafion/sulfated titania membranes for PEMFCs. *Int. J. Hydrogen Energy* **2015**, *40*, 14651–14660. [[CrossRef](#)]
95. Enotiadis, A.; Boutsika, L.G.; Spyrou, K.; Simari, C.; Nicotera, I. A facile approach to fabricating organosilica layered material with sulfonic groups as an efficient filler for polymer electrolyte nanocomposites. *New J. Chem.* **2017**, *41*, 9489–9496. [[CrossRef](#)]
96. Nicotera, I.; Simari, C.; Boutsika, L.G.; Coppola, L.; Spyrou, K.; Enotiadis, A. NMR investigation on nanocomposite membranes based on organosilica layered materials bearing different functional groups for PEMFCs. *Int. J. Hydrogen Energy* **2017**, *42*, 27940–27949. [[CrossRef](#)]
97. Xu, L.; Yang, L.; Johansson, E.M.J.; Wang, Y.; Jin, P. Photocatalytic activity and mechanism of bisphenol a removal over TiO<sub>2</sub>-x/rGO nanocomposite driven by visible light. *Chem. Eng. J.* **2018**, *350*, 1043–1055. [[CrossRef](#)]
98. Reddy, P.V.L.; Kim, K.H.; Kavitha, B.; Kumar, V.; Raza, N.; Kalagara, S. Photocatalytic degradation of bisphenol A in aqueous media: A review. *J. Environ. Manag.* **2018**, *213*, 189–205. [[CrossRef](#)]
99. Garg, A.; Singhania, T.; Singh, A.; Sharma, S.; Rani, S.; Neogy, A.; Yadav, S.R.; Sangal, V.K.; Garg, N. Photocatalytic Degradation of Bisphenol-A using N, Co Codoped TiO<sub>2</sub> Catalyst under Solar Light. *Sci. Rep.* **2019**, *9*, 765. [[CrossRef](#)]

**Disclaimer/Publisher’s Note:** The statements, opinions and data contained in all publications are solely those of the individual author(s) and contributor(s) and not of MDPI and/or the editor(s). MDPI and/or the editor(s) disclaim responsibility for any injury to people or property resulting from any ideas, methods, instructions or products referred to in the content.